



**HAL**  
open science

## Magnetochrome-catalyzed oxidation of ferrous iron by MamP enables magnetite crystal growth in the magnetotactic bacterium AMB-1

Matthieu Amor, Daniel Chevrier, Marina I. Siponen, Ramon Egli, Ernesto Scoppola, Lourdes Marcano, Chenghao Li, Damien Faivre, Fadi Choueikani

► **To cite this version:**

Matthieu Amor, Daniel Chevrier, Marina I. Siponen, Ramon Egli, Ernesto Scoppola, et al.. Magnetochrome-catalyzed oxidation of ferrous iron by MamP enables magnetite crystal growth in the magnetotactic bacterium AMB-1. *Proceedings of the National Academy of Sciences of the United States of America*, 2024, 121 (50), pp.e2410245121. 10.1073/pnas.2410245121 . hal-04828114

**HAL Id: hal-04828114**

**<https://hal.science/hal-04828114v1>**

Submitted on 10 Dec 2024

**HAL** is a multi-disciplinary open access archive for the deposit and dissemination of scientific research documents, whether they are published or not. The documents may come from teaching and research institutions in France or abroad, or from public or private research centers.

L'archive ouverte pluridisciplinaire **HAL**, est destinée au dépôt et à la diffusion de documents scientifiques de niveau recherche, publiés ou non, émanant des établissements d'enseignement et de recherche français ou étrangers, des laboratoires publics ou privés.

1 **Magnetochrome-catalyzed oxidation of ferrous iron by MamP**  
2 **enables magnetite crystal growth in the magnetotactic**  
3 **bacterium AMB-1**

4  
5  
6 Matthieu Amor<sup>1,2\*</sup>, Daniel M. Chevrier<sup>1</sup>, Marina I. Siponen<sup>1</sup>, Ramon Egli<sup>3</sup>, Ernesto  
7 Scoppola<sup>4</sup>, Lourdes Marcano<sup>5,6</sup>, Chenghao Li<sup>4</sup>, Fadi Choueikani<sup>7</sup>, Damien Faivre<sup>1\*</sup>

8  
9  
10  
11 <sup>1</sup> Aix-Marseille Université, CEA, CNRS, BIAM, 13115 Saint-Paul-lez-Durance, France

12  
13 <sup>2</sup> Univ. Lyon, ENSL, UCBL, UJM, CNRS, LGL-TPE, 69007 Lyon, France

14  
15 <sup>3</sup> Department of Geophysics, Geosphere, Vienna, Austria

16  
17 <sup>4</sup> Biomaterials, Hierarchical Structure of Biological and Bio-inspired Materials, Max  
18 Planck Institute of Colloids and Interfaces, 14476 Potsdam, Germany

19  
20 <sup>5</sup> Center for cooperative research in biomaterials (CIC biomaGUNE), Basque research  
21 and technology alliance (BRTA), Paseo de Miramón 194, Donostia-San Sebastián  
22 20014, Spain

23  
24 <sup>6</sup> Department of Physics & MAGNES, University of Oviedo, 33007 Oviedo, Spain

25  
26 <sup>7</sup> Synchrotron SOLEIL, L'Orme des Merisiers, 91190 Saint-Aubin, France

27  
28  
29 \*Corresponding authors:

30 [matthieu.amor@ens-lyon.fr](mailto:matthieu.amor@ens-lyon.fr) (MA); [damien.favre@cea.fr](mailto:damien.favre@cea.fr) (DF)

31  
32  
33 Keywords: Magnetotactic bacteria, Cytochromes, Magnetite biomineralization,  
34 Magnetotaxis

## 38 **Abstract**

39 Magnetotactic bacteria have evolved the remarkable capacity to biomineralize chains of  
40 magnetite [Fe(II)Fe(III)<sub>2</sub>O<sub>4</sub>] nanoparticles that align along the geomagnetic field and  
41 optimize their navigation in the environment. Mechanisms enabling magnetite formation  
42 require the complex action of numerous proteins for iron acquisition, sequestration in  
43 dedicated magnetosome organelles, and precipitation into magnetite. The MamP protein  
44 contains c-type cytochromes called magnetochrome domains that are found exclusively in  
45 magnetotactic bacteria. Ablation of magnetochromes in MamP prevents bacteria from  
46 aligning with external magnetic fields, showing their importance to maintain this biological  
47 function. MamP has been proposed, mostly from *in vitro* experimentations, to regulate iron  
48 redox state and maintain an Fe(II)/Fe(III) balance compatible with magnetite formation via  
49 the iron oxidase activity of magnetochromes. To test the proposed function for MamP *in*  
50 *vivo* in the magnetotactic strain AMB-1, we characterized the iron species in chemical  
51 MamP-mediated magnetite syntheses as well as in bacteria unable to produce MamP using a  
52 combination of physico-chemical methodologies. We show that MamP has no apparent  
53 control on the speciation and oxidation state of intracellular iron nor on the Fe(II)/Fe(III)  
54 balance in magnetite. We propose that MamP promotes magnetite growth by incorporating  
55 Fe(III) into pre-existing magnetite seeds, and that magnetite structure and stoichiometry is  
56 maintained by further equilibration with dissolved Fe(II) in magnetosome organelles.

57

## 58 **Significance**

59 Biological organisms can produce crystalline structures via biomineralization.  
60 Magnetotactic bacteria synthesize chains of iron-based magnetic nanoparticles

61 (magnetite) in magnetosome organelles to magnetically orient in aquatic environments.  
62 Many proteins are involved in this process to tightly control the nanoparticle properties.  
63 Here, we resolve the function of MamP, a particularly important protein that contains c-  
64 type cytochrome-like motifs specific to magnetotactic bacteria called magnetochromes.  
65 We demonstrate that MamP enables proper growth of magnetite nanoparticles to optimize  
66 the magnetic properties of magnetite, which is critical for magnetic orientation to  
67 maintain the biological function. These results also establish MamP as a promising  
68 candidate for generating isotope anomalies that are used for reconstructing the emergence  
69 of magnetotactic bacteria on Earth.

## 70 **Introduction**

71 Biological organisms have evolved the capacity to form crystalline structures from  
72 inorganic ions. This process, termed biomineralization, is widespread among both  
73 prokaryotes and eukaryotes and serve specific biological functions. Magnetotactic bacteria  
74 (MTB) are the only known microorganisms synthesizing intracellular ferrimagnetic  
75 nanoparticles made of either magnetite [Fe(II)Fe(III)<sub>2</sub>O<sub>4</sub>] or greigite [Fe(II)Fe(III)<sub>2</sub>S<sub>4</sub>] in a  
76 genetically controlled manner (1). They are ubiquitous in all types of aquatic environments,  
77 and are thought to have emerged on Earth at least ~3 billion years ago (2). In MTB, a single  
78 nanoparticle is contained within organelles called magnetosomes, which consist of lipid  
79 vesicles surrounding the magnetite or greigite crystal (3). The nanoparticle size is restricted  
80 to fall within the magnetic stable single-domain range, optimizing the magnetic contribution  
81 of each iron atom. The chain alignment of magnetosomes also maximizes the cell's  
82 magnetic anisotropy and provides a stable magnetic moment to the bacteria. It is assumed  
83 that magnetosome chains are used for passive alignment along the geomagnetic field to  
84 optimize the search for suitable redox conditions in chemically stratified environments.

85 In magnetite-forming MTB, genetic factors are responsible for the stepwise magnetosome  
86 formation: the invagination of magnetosome vesicles from the inner cell membrane, the  
87 alignment of magnetosomes along cytoskeletal filaments, the iron delivery to magnetosomes  
88 for magnetite precipitation, and the crystal growth and maturation. The redox state of  
89 intracellular iron has to be tightly controlled to allow for storage, solubilization, delivery to  
90 the magnetosomes, and magnetite formation (3). MamP has been proposed as a key protein  
91 for controlling the Fe(II)/Fe(III) balance in magnetosomes (4, 5). It is highly conserved in  
92 known magnetite-forming MTB (3), and is embedded within the magnetosome membrane.

93 MamP comprises two magnetochrome domains (Pfam: PF18509), a c-type cytochrome-like  
94 domain specific to MTB consisting of double CXXCH heme motifs facing the magnetosome  
95 lumen and predicted to function as Fe(II) oxidases (4–6). Gene deletion of *mamP* in model  
96 strains severely impairs biomineralization with typically one large magnetite crystal per cell  
97 accompanied by many small (<10 nm) flake-shaped particles (1, 5). Electron microscopy  
98 characterizations of single particles showed that the fraction of these small nanoparticles  
99 possessing a resolved lattice structure are compatible with magnetite, but the presence of  
100 distinct and potentially amorphous iron phases in the small nanoparticle population remains  
101 unclear (5). MamP activity was shown to be magnetochrome-dependent (5). Finally, MamP  
102 is able to form magnetite nanoparticles from ferrous iron only under basic pH conditions in  
103 aqueous solutions by partially oxidizing  $\text{Fe}^{2+}$  and subsequently allowing  $\text{Fe}^{2+}/\text{Fe}^{3+}$  co-  
104 precipitation similarly to what is commonly observed during chemical precipitation of  
105 magnetite nanoparticles (4, 5).

106 Major responses regarding MamP function(s) have mostly been obtained *in vitro* and thus  
107 remain to be elucidated *in vivo*. For example, the capacity of MamP to maintain a fixed  
108 Fe(II)/Fe(III) ratio close to that of magnetite in magnetosomes has not been demonstrated.  
109 The potential involvement of MamP in maintaining the nanoparticle size within the stable  
110 magnetic single-domain range also remains to be resolved. Finally, the presence of  
111 magnetite precursors, which could be triggered by MamP activity, and their importance for  
112 biomineralization have been largely debated (7–9). In this contribution, we characterized the  
113 mineral phases and iron species in bacterial and magnetite samples through physico-  
114 chemical approaches (electron microscopy, magnetic measurements, X-ray diffraction, X-  
115 ray absorption spectroscopy and X-ray magnetic circular dichroism) enabling measurements

116 at the bulk level, thus avoiding biases induced by a limited number of magnetite  
117 nanoparticles and/or bacteria. Four types of samples were analyzed: nanoparticles produced  
118 chemically from Fe<sup>2+</sup> and Fe<sup>3+</sup> ions, nanoparticles produced from Fe<sup>2+</sup> in the presence of  
119 MamP, wild-type MTB and their particles produced biologically, as well as bacterial MamP  
120 genetic knockouts and their nanoparticles. Our results do not support the proposed function  
121 of MamP in controlling the Fe(II)/Fe(III) balance for magnetite formation: iron is  
122 qualitatively and quantitatively found in the same chemical species and oxidation states in  
123 mutant bacteria lacking MamP. They rather point towards a MamP-controlled magnetite  
124 growth by partial oxidation of ferrous iron entering magnetosomes and addition of the  
125 resulting Fe(III) to pre-existing nanoparticles. The present contribution establishes an  
126 updated function of the magnetochrome domain and shows that detailed characterization of  
127 the mineral products in MTB helps unravelling the biochemical reactions catalyzed by  
128 biomineralization proteins.

129

## 130 **Results**

### 131 **Crystal production in chemical and biological syntheses**

132 Inorganic magnetite nanoparticles, hereafter referred to as chemical magnetite, were  
133 synthesized by Fe<sup>2+</sup>/Fe<sup>3+</sup> co-precipitation in aqueous solution at constant pH = 9 compatible  
134 with the biomineralization medium (10), following an established method (11) (Fig. S1). X-  
135 ray diffraction (XRD) analyses showed all typical peaks of magnetite (12) and confirmed the  
136 crystal purity in this sample (Fig. 1A). The wild-type magnetotactic strain *Magnetospirillum*  
137 *magneticum* AMB-1 (hereafter referred to as WT AMB-1; Fig. S1) yielded the same  
138 diffraction peaks with positions attributed to magnetite, also showing that AMB-1 produced

139 magnetite as the sole crystalline product (Fig. 1A). Chemical magnetite yielded broader  
140 peaks due to the smaller crystallite sizes (see below). To test the ability of MamP to produce  
141 magnetite from  $\text{Fe}^{2+}$ , we performed *in vitro* syntheses of magnetite nanoparticles (hereafter  
142 referred to as MamP magnetite) in an aqueous solution by mixing MamP and dissolved  $\text{Fe}^{2+}$   
143 under anoxic conditions at pH = 9 (Fig. S1). The precipitation solution possessed a dark  
144 green color compatible with a mixture of green rust and magnetite (Fig. S2). The  
145 precipitation solution immediately turned orange upon exposure to air for sample recovery  
146 and drying (Fig. S2), which could be explained by green rust oxidizing into (oxy)hydroxides  
147 such as ferrihydrite and/or goethite likely originating from excess Fe(II) (see supporting  
148 text). To limit sample oxidation, MamP magnetite was immediately stored in vacuum upon  
149 recovery without rinsing with Milli-Q water. The mineralogical composition of MamP  
150 magnetite samples showed spatial heterogeneities, but the presence of magnetite, halite and  
151 goethite was confirmed by XRD (Figs. 1A, S3 & S4). Sample manipulation with a magnetic  
152 separator (MACSiMAG, Miltenyi Biotec) could not separate magnetite from organic  
153 material and goethite, likely because of magnetite encapsulation in co-occurring material  
154 (Fig. S1). Given that oxidation and dissolution of magnetite occur during digestion of  
155 organic matter and goethite dissolution, MamP magnetite was not further processed to allow  
156 characterization of native magnetic properties (see below and supporting information).  
157 Finally, the crystalline products of mutant AMB-1 bacteria unable to produce MamP  
158 (hereafter referred to as  $\Delta\text{mamP}$  AMB-1) were determined. The low crystal content yielded  
159 smaller diffraction peaks, with only the most intense (311) reflection of magnetite observed  
160 (Fig. 1B).

161 XRD peak refinement was used to calculate the magnetite crystallite sizes (Fig. S5).

162 MamP generated smaller nanocrystals ( $8.5 \pm 1.2$  nm) than the pure chemical synthesis ( $10.8$   
163  $\pm 0.2$  nm). The two AMB-1 strains yielded indistinguishable XRD crystallite sizes:  $29.2 \pm$   
164  $0.3$  and  $28.2 \pm 2.3$  nm for WT and  $\Delta mamP$  AMB-1, respectively. However, magnetic  
165 characterization results discussed below clearly excluded a comparable size for magnetite  
166 produced in the two AMB-1 strains, which is compatible with the lower particle size  
167 reported for  $\Delta mamP$  bacteria (1, 13). In addition, X-ray absorption spectroscopy (XAS)  
168 pointed to highly similar iron species and their relative fractions in the two bacterial samples  
169 (see below). It is known that XRD peak refinement is biased towards larger crystallite sizes  
170 when two populations of particles coexist (14). Therefore, the large fraction of nanoparticles  
171 below 10 nm in the mutant strain is likely to have been neglected by XRD.

172

### 173 **Iron in chemical and bacterial samples: speciation, coordination, oxidation state and** 174 **magnetic properties**

175 Iron speciation was characterized in all samples by X-ray absorption spectroscopy (XAS)  
176 at the Fe  $L_{2,3}$ -edges to determine the role of MamP in controlling the iron redox state during  
177 biomineralization. In addition, X-ray magnetic circular dichroism (XMCD) spectra were  
178 acquired using fully polarized photons (right and left polarizations) to further distinguish  
179 iron oxides and species by their intrinsic magnetic properties (materials and methods).  
180 Unless otherwise specified, all data were acquired at a temperature of 3 K.

181 XAS spectra corresponding to WT and  $\Delta mamP$  AMB-1 were strikingly similar, yielding  
182 comparable  $L_{3-a}$  and  $L_{3-b}$  peak positions and relative intensities (Figs. 2A-2D) (Table S1).  
183 Chemical magnetite alone could not fit the bacterial samples: the  $L_{3-b}$  peak and the rising  
184  $L_{3-a}$  edge were shifted towards higher energies in bacterial samples, indicative of a larger

185 weight for the ferric species. In addition, the  $L_{3-b}/L_{3-a}$  intensity peak ratio was higher in  
186 bacteria, also indicative of a more oxidized state for iron in the biological samples (15). We  
187 calculated linear combinations of reference samples (Fig. S6) to fit the composition of each  
188 bacterial strain. The combination of iron species best matching AMB-1 samples was a  
189 mixture of magnetite (30 %), maghemite (40 %) and ferrihydrite (30 %) (Figs. 2B & 2D). A  
190 ferrihydrite fraction of 30 % in AMB-1 is in line with the reported values (8, 16, 17).  
191 Magnetotactic strains including AMB-1 are also known to produce non-stoichiometric  
192 magnetite, with an Fe(II)/Fe(III) ratio below 0.5 and pointing to partial maghemitization  
193 (18). Potentially unidentified phases could also contribute to the XAS spectra of bacteria,  
194 but the proposed combination of magnetite, maghemite and ferrihydrite is thus compatible  
195 with the established iron budget of MTB cells as well as distinct XAS data previously  
196 acquired on MTB (17).

197 Given their oxidase activity, magnetochromes were assumed to contain iron in its  
198 oxidized form (4–6). Over subsequent XAS measurements, the  $L_{3-b}/L_{3-a}$  intensity peak  
199 ratios of MamP proteins decreased from 5 to 1.25 showing a progressive reduction of Fe(III)  
200 contained in magnetochromes into Fe(II) (Fig. S7). MamP magnetite samples did not show  
201 this beam-induced reduction behavior, which could suggest that co-occurring chemical  
202 species protected MamP from beam damage and/or that iron atoms in MamP magnetite  
203 would have incorporated into mineral structures limiting significant beam-induced chemical  
204 change. The acquired spectra of MamP magnetite also showed dissimilarities with chemical  
205 magnetite: the  $L_{3-b}$  peak position was shifted towards higher energies and the  $L_{3-b}/L_{3-a}$   
206 intensity peak ratio was higher than chemical magnetite (Fig. 2E) (Table S1). To assess  
207 whether goethite identified from XRD could explain the discrepancies between chemical and

208 MamP magnetite, we calculated linear combinations of reference samples (only the first  
209 acquired spectrum for MamP proteins was used as representative reference). Experimental  
210 data obtained from MamP magnetite showed the best fit with a mixing of maghemite (55%),  
211 goethite (37%) and MamP proteins (8%) (Fig. 2F).

212 Iron valence and site occupancy, either tetrahedral ( $T_d$ ) or octahedral ( $O_h$ ), were further  
213 characterized with XMCD (Figs. 3 & S8). Chemical magnetite, WT and  $\Delta mamP$  AMB-1  
214 possessed a large magnetic contribution (Figs. 3A & 3B). Following the methodology of  
215 Jungcharoen and co-workers (19), the  $Fe^{2+}O_h : Fe^{3+}T_d : Fe^{3+}O_h$  peak ratios were used to  
216 show that chemical magnetite stoichiometry slightly deviates from pure magnetite with < 10  
217 % maghemite composition that could have been generated by a limited magnetite oxidation  
218 during sample storage and/or mounting on the sample holder (Fig. 3A) (Table S2).  
219 Importantly, partial oxidation does not alter the interpretation of our experimental results  
220 and XAS linear combinations as stoichiometric magnetite alone could not account for the  
221 XAS spectra. The small degree of oxidation seen in XMCD is consistent with our XAS data  
222 of MamP magnetite and bacterial samples, which can be explained by stoichiometric  
223 magnetite and a contribution of additional ferric iron in octahedral configuration. In the case  
224 of the two bacterial strains, XMCD indicates the coexistence of  $Fe^{2+}$  and  $Fe^{3+}$  in tetrahedral  
225 and octahedral configurations with a dominant presence of  $Fe^{3+}O_h$  compatible with distinct  
226 oxidized iron phases identified from XAS (Table S2). Still, WT AMB-1 had a  $Fe^{3+}T_d$   
227 contribution comparable to that of magnetite, likely pointing to the higher amount of  
228 magnetite in this strain as compared to  $\Delta mamP$  AMB-1 (Figs. S1) (1, 13). Finally, MamP  
229 magnetite showed a lower magnetic contrast, which points to a more dilute nature of  
230 ferrimagnetic materials (Figs. 3D & S1, Table S3). The relative peak intensities indicated a

231 high contribution of  $\text{Fe}^{3+}\text{O}_h$ , in line with the presence of goethite identified from XRD  
232 (Table S2).

233 Paramagnetic and/or antiferromagnetic species should have no net magnetic moment at  
234 room temperature. Accordingly, their XMCD signature is expected to decrease as the  
235 temperature increases. We thus carried out additional measurements of bacterial samples at  
236 300 K to further isolate the XMCD contribution of magnetite from other intracellular iron  
237 species. As expected for paramagnetic species, the magnetic contrast of bacteria decreased at  
238 300 K (Figs. 3B & 3C). The concurrent decrease and increase of the relative contributions of  
239  $\text{Fe}^{3+}\text{O}_h$  and  $\text{Fe}^{3+}\text{T}_d$ , respectively, at 300 K is also in line with XMCD specifically probing  
240 magnetite (Table S2). Under these conditions, the XMCD spectra of the two AMB-1 strains  
241 became almost indistinguishable with only the  $\text{Fe}^{2+}\text{O}_h$  peak slightly larger in  $\Delta\text{mamP}$  AMB-  
242 1 (variation of the  $\text{Fe}^{2+}\text{O}_h$  relative contribution between the two strains of less than 1 %, see  
243 Table S2), showing that magnetite stoichiometry in the two bacterial samples was highly  
244 similar.

245

#### 246 **Magnetic properties and chain structure of magnetite**

247 FORC (first-order reversal curves) analyses were performed to further elucidate the  
248 function of MamP. A FORC diagram represents magnetic hysteresis properties in terms of a  
249 joint distribution  $\rho(B_c, B_u)$  of squared hysteresis loops with half-width  $B_c$  (also known as  
250 coercivity) and offset field  $B_u$  (20). XRD indicated magnetite as the sole contributor to the  
251 sample magnetization (Fig. 1), except for MamP magnetite sample also containing the  
252 antiferromagnetic goethite. Goethite is easily distinguishable from magnetite because of its  
253 large coercivity ( $> 300$  mT, ref. 21). Accordingly, this mineral, which is also characterized

254 by a spontaneous magnetization  $> 2$  orders of magnitude smaller than that of magnetite ( $< 1$   
255 vs.  $\sim 90 \text{ Am}^2 \text{ kg}^{-1}$ , ref. 22), is not expected to contribute to the FORC measurements over the  
256 used field range. The magnetite crystal size of all samples is sufficiently small to ensure that  
257 all particles contain a single magnetic domain with nearly homogeneous magnetization (23).  
258 Accordingly, the FORC diagrams of Fig. 4 are simply interpretable as the joint distributions  
259 of coercivities ( $B_c$ ) and local biasing fields ( $B_u$ ) caused by magnetic interactions (20) for the  
260 fraction of single particles (chemical and MamP magnetite) and chains of particles (WT and  
261  $\Delta mamP$  AMB-1) that are sufficiently large for their magnetization to be stable within the  
262 measurement time. This is known as the stable single-domain fraction (SSD), as opposed to  
263 smaller superparamagnetic (SP) particles, which do not contribute to the FORC diagram  
264 owing to their lack of hysteresis. The SP-SSD limit for magnetite particles is comprised  
265 between  $\sim 11$  and  $\sim 20$  nm for shape factors compatible with AMB-1 magnetite (24). Particles  
266 with sizes close to the SP-SSD limit display time-dependent magnetic properties (magnetic  
267 viscosity) resulting in a vertical ridge along  $B_c = 0$  (20).

268 The FORC signature of chemical magnetite (Fig. 4A) was very similar to that of  
269 thermally activated spin glasses, which are systems of magnetic spins with disordered  
270 magnetic couplings subjected to thermal perturbations (25). In the case of chemical  
271 magnetite, spins were represented by the magnetic moments of individual crystals, and  
272 disordered magnetic couplings arose from magnetostatic interactions within closely packed,  
273 random clusters (Fig. S1). Magnetic viscosity was also indicated by the presence of a  
274 vertical ridge along  $B_c = 0$ . MamP magnetite had a similar signature (Fig. 4B). However, the  
275 vertical spread of the FORC distribution was significantly reduced in comparison to  
276 chemical magnetite, converging to a horizontal ridge running slightly above  $B_u = 0$ . This so-

277 called central ridge (CR), which, in its sharpest version, is clearly visible in the AMB-1  
278 samples (Figs. 4C & 4D), is the characteristic signature of isolated SD particles or linear  
279 chains of such particles (20). Its presence is consistent with a more dispersed nature of  
280 MamP crystals than chemical magnetite (Fig. S1). We tentatively propose that MamP  
281 magnetite passively nucleated on the surface of the organic materials, which increased the  
282 number of nucleation events (smaller particle sizes for a given amount of iron) and  
283 prevented particle clustering. The smaller particle size of MamP magnetite could also be  
284 explained by the lower iron concentration used in the *in vitro* syntheses, which was required  
285 to enable a sufficient fraction of ferrous iron to be oxidized given the quantity of MamP  
286 proteins that could be produced (see materials and methods). The much closer hysteresis  
287 loop of MamP magnetite relative to chemical magnetite clearly indicated that most particles  
288 are SP (Fig. S1).

289 FORC diagrams of MTB are dominated by the presence of a sharp central ridge, along  
290 with a symmetric pair of positive and negative lobes in the lower quadrant, which are the  
291 typical signatures of isolated SSD particles or chains of particles. In contrast with chemical  
292 and MamP magnetite, hysteresis loops are much more opened, as expected for SSD particle  
293 assemblages (20). WT AMB-1 showed all features characteristic of MTB cultures (Fig. 4D),  
294 including a faint vertical ridge reflecting a minor contribution of viscous particles that are  
295 commonly observed in MTB cultures (26). The magnetic properties of  $\Delta mamP$  AMB-1 were  
296 qualitatively similar to that of WT AMB-1 (Fig. 4C), including a vertical ridge from viscous  
297 particles. The only significant difference between the two samples was the lower coercivity  
298 of  $\Delta mamP$  bacteria ( $B_c = 8.1$  mT vs. 17.8 mT), which was also reflected by the median of  
299 the CR coercivity distribution ( $\sim 14$  mT vs.  $\sim 32$  mT). This difference can be explained by a

300 combination of (i) a lower average particle size, (ii) higher shape factors, and (iii) a lower  
301 superimposed axial anisotropy from the chain structure, owing to the much larger in-chain  
302 distances between individual crystals (27).

303 For any size distribution crossing the SP-SSD boundary, only a small fraction of the  
304 particles contributes to the vertical ridge. Therefore, this ridge cannot be used as a  
305 quantification of SP magnetite. Given the single-domain nature of the investigated materials,  
306 the remanent saturation ( $M_{rs}$ ) to saturation magnetization ( $M_s$ ) can be used to estimate the  
307 SSD fraction, considering  $M_{rs}/M_s = 0.5$  for the 100% SSD endmember in the case of well-  
308 dispersed particles, and  $M_{rs}/M_s = 0$  for the SP endmember (28). WT AMB-1 possessed an  
309  $M_{rs}/M_s$  ratio (0.470) close to but lower than the ideal value of 0.5 for chains of stable single-  
310 domain particles, confirming the presence of some growing superparamagnetic magnetite in  
311 MTB cultures (26, 28). The decrease of  $M_{rs}/M_s$  to 0.443 in  $\Delta mamP$  AMB-1 was consistent  
312 with a relative increase of SP magnetite in this strain. Assuming  $M_{rs}/M_s$  to be a linear  
313 combination of the SSD and SP endmembers, we estimate the volume fraction of SP  
314 magnetite to be ~6 % and ~11 % in WT and  $\Delta mamP$  AMB-1 respectively. To further  
315 validate results obtained from FORC, the particle size and shape factor ( $S$ , defined as  $S =$   
316 width/length) of magnetite produced by bacteria was measured from electron microscopy  
317 (Fig. 5 & Table 1). The mean length of magnetite produced by WT and  $\Delta mamP$  bacteria was  
318 39 and 21 nm respectively, in good agreement with publications investigating WT and  
319  $\Delta mamP$  AMB-1 as well as distinct magnetotactic strains (5, 13, 29–31). Particle size  
320 obtained from XRD was lower in both cases, which has previously been reported (32). The  
321 explanation for this discrepancy is that XRD is sensitive to an effective volume measured in  
322 a specific vector, while particle sizes with electron microscopy are calculated from a

323 projected three-dimensional structure. Overall, electron microscopy observations of AMB-1  
324 bacteria are compatible with FORC considering the potential biases induced by two-  
325 dimensional projections of three-dimensional objects, and yielded ~2 % (WT AMB-1) and  
326 ~14 % ( $\Delta mamP$  AMB-1) of SP magnetite (see supporting text). This demonstrates that all  
327 flake-shaped particles in  $\Delta mamP$  AMB-1 correspond to magnetite. Chemical and MamP  
328 magnetite had much lower  $M_{rs}/M_s$  ratios of 0.085 and 0.012, respectively, in line with both  
329 small magnetite sizes contained within the SP domain and the clustered particle organization  
330 (28, 33).

331

## 332 **Discussion**

333 Magnetite biomineralization in MTB is a remarkable process requiring the action of  
334 numerous proteins. Among them, MamP is one of the few magnetosome proteins highly  
335 conserved in magnetite-forming MTB, illustrating its importance (3). MamP is abundant in  
336 the magnetosome membrane (34), with magnetochrome domains facing the magnetosome  
337 lumen (4, 6). Iron is known to be homogeneously delivered to all magnetosomes in the form  
338 of labile  $Fe^{2+}$  crossing the magnetosome membrane, and this mechanism is not impaired in  
339 AMB-1 cells lacking MamP (13, 35). Our experimental results allow the proposal of a  
340 model for MamP function in AMB-1 magnetite biomineralization (Fig. 6), and enables  
341 speculation about MamP function in diverse MTB. According to this model, Fe(II) first  
342 entering empty magnetosome vesicles is nucleated as magnetite through the action of  
343 nucleating proteins. For instance, MamO has been shown to be required for the initiation of  
344 magnetite biomineralization by directly binding iron atoms (36). In addition, templating  
345 proteins such as MamC could promote nucleation and initial growth of magnetite seeds (37).

346 The small size of magnetosome vesicles at the stage of crystal nucleation (38) also increases  
347 the magnetite saturation index to thermodynamically favor  $\text{Fe}^{2+}_{(\text{aq})}$  precipitation into  
348 magnetite under the basic ( $7.5 < \text{pH} < 9.5$ ) and reductive ( $-0.25 < \text{Eh} < -0.60 \text{ V}$ ) conditions  
349 in magnetosomes (10). Subsequently, MamP enables magnetite growth via magnetochromes  
350 (5) by partially oxidizing ferrous iron entering the magnetosome and incorporating Fe(III)  
351 into the pre-existing nanoparticles. The absence of magnetosome vesicles confining iron into  
352 a restricted volume in the *in vitro* syntheses also explains the lower particle sizes achieved in  
353 MamP magnetite as compared to those observed in WT AMB-1, which allows iron oxidized  
354 by MamP to freely react with ferrous iron and increases the number of nucleation events in  
355 the entire solution volume. Nucleation of magnetite in  $\Delta\text{mamP}$  AMB-1 suggests that MamP  
356 activity does not induce the formation of magnetite precursors, although alternative  
357 biomineralization pathways might be triggered in the absence of MamP (8). Still, magnetite  
358 crystals produced in  $\Delta\text{mamP}$  AMB-1 did not yield shape factors compatible with those  
359 found in WT bacteria, which points to a lower particle elongation in bacteria lacking MamP  
360 (Fig. 5 & Table 1). Even if no direct experimental evidence for asymmetrical distribution of  
361 MamP in magnetosome vesicles exist, the only hypothesis we can propose to resolve these  
362 observations is that MamP is anchored on one side of the magnetosome vesicle only, and  
363 thus adds iron to magnetite on one side of the nanoparticle, which decreases the shape factor.  
364 We note that MamP is required to generate ferric iron species (i.e., magnetite) in the *in vitro*  
365 syntheses: no oxidation of Fe(II) occurs in the absence of MamP (4, 5). Combined with the  
366 iron oxidase activity predicted for MamP magnetochromes (4, 6), these evidences strongly  
367 support Fe(III) to be the product of MamP activity. As a result, hemes contained in  
368 magnetochromes would become reduced and electron transfer to putative electron acceptors

369 would be required to enable further iron oxidation by MamP. The presence of a respiratory  
370 chain in the magnetosome membrane could provide a satisfactory mechanism to fulfill such  
371 electron transfer (6). Oxidized compounds including nitrates could also serve as electron  
372 acceptors (39). Alternatively, no secondary oxidation of MamP would be required to  
373 promote further iron oxidation if newly synthesized MamP proteins are addressed to  
374 magnetosomes at a sufficient rate to sustain magnetite expansion. Finally, residual Fe(II) in  
375 the magnetosome vesicle becomes available for adsorbing on the growing nanoparticle. In  
376 this case, the magnetite lattice serves as a template so that adsorbing Fe(II) further  
377 precipitates into magnetite to preserve the crystal structure. This mechanism has been  
378 evidenced in Fe(II)-oxidizing bacteria which can trigger magnetite expansion through iron  
379 oxidation only when magnetite seeds are initially present (40). Electron transfer from  
380 adsorbed Fe(II) to the particle core could also occur to keep the Fe(II)/Fe(III) ratio  
381 homogeneous and consistent with magnetite (Fig. 3C), again similar to what has been  
382 observed during iron oxide biomineralization in iron-metabolizing bacteria (41).

383 We note that 10 % of magnetite crystals in  $\Delta mamP$  AMB-1 possessed sizes compatible  
384 with stable single-domain particles similar to those of WT AMB-1 (Fig. 5 & Table 1). Such  
385 observation demonstrates that, in some cases, magnetite grows up to fully mature sizes  
386 without MamP. This shows that the small nanoparticle size in  $\Delta mamP$  bacteria cannot be  
387 explained by a small vesicle volume restricting magnetite expansion (38). Still, these mature  
388 particles in  $\Delta mamP$  AMB-1 displayed higher shape factors (Fig. 5) than WT AMB-1  
389 magnetite pointing to a more isotropic growth when MamP is lacking. The presence of only  
390 a few large crystals in  $\Delta mamP$  cells can be explained by kinetic effects: magnetite is  
391 predicted to be the thermodynamically stable phase when considering dissolved Fe(II) under

392 the expected chemical conditions encountered in magnetosomes (10). MamP can act as a  
393 catalyst to increase the reaction rate of magnetite formation. Such kinetic effects are  
394 supported by a positive linear correlation between the number of large crystals and the  
395 number of total particles in a single  $\Delta mamP$  cell (Fig. 7) (i.e., more large crystals when the  
396 intracellular iron concentration is expected to be high, ref. 37). Alternatively, distinct  
397 magnetosome proteins can possess redundant functions with MamP to partially maintain  
398 iron oxidation for magnetite growth. Magnetochrome-containing MamT and MamX are  
399 obvious candidates, although gene deletion of *mamX* in the MSR-1 strain generated oxidized  
400 products, suggesting an iron reductase activity for MamX (43). In addition, MamT was  
401 proposed to regulate the magnetosome vesicle size (44). Interplay between magnetosome  
402 proteins is supported by the recent finding of magnetosome genes also regulating the  
403 nanoparticle elongation in AMB-1 (45). These two scenarios (kinetic effects and proteins  
404 with redundant function) are not mutually exclusive.

405 Overall, the results described in this work modify the established scheme defining MamP  
406 as a regulator of the Fe(II)/Fe(III) balance in AMB-1 cells and their magnetosomes.  
407 Magnetic characterizations and XAS analyses demonstrated that iron speciation and  
408 oxidation state remain qualitatively and quantitatively unchanged upon *mamP* gene deletion  
409 (Figs. 2 & 4). Furthermore, XMCD pointed to magnetite with highly similar  
410  $Fe^{2+}O_h:Fe^{3+}T_d:Fe^{3+}O_h$  ratios in the two bacterial strains and their magnetite nanoparticles  
411 (Fig. 3C; Table S2). The present contribution establishes MamP and its magnetochromes as  
412 key factors controlling magnetite crystal growth in AMB-1 up to sizes falling within the  
413 stable single-magnetic domain required to generate large magnetic moments and enabling  
414 interactions with external magnetic fields. Future studies should determine whether distinct

415 magnetochrome-containing proteins such as MamT or MamX possess a similar function.

416

## 417 **Methods**

### 418 **Cultivation of AMB-1 strains**

419 *Magnetospirillum magneticum* AMB-1 (ATCC 700264) was cultivated following the  
420 protocol described by Komeili and co-workers (46). The sole iron source provided to AMB-  
421 1 cultures corresponded to Fe(III)-citrate at 100  $\mu$ M.  $\Delta$ *mamP* AMB-1 cells were provided by  
422 Pr. Arash Komeili. They were produced following a published protocol (1), and cultivated in  
423 the same experimental conditions as wild-type AMB-1.

424

### 425 **Cloning, protein production and purification**

426 The DNA sequence corresponding to residues D26-Q260 of magnetotactic ovoidal  
427 bacterium MO-1 *mamP* gene was sub-cloned into the plasmid pET26b+ (Novagen), as  
428 previously published (4). The detailed procedure for MamP production is provided in the  
429 supporting information.

430

### 431 **Synthesis of chemical and MamP magnetite samples**

432 Production of magnetite nanoparticles was performed using a titration device (Metrohm) as  
433 already described (11). For chemical magnetite, an iron chloride mixture ( $[\text{Fe(II)Cl}_2] = 0.33$   
434 M and  $[\text{Fe(III)Cl}_3] = 0.66$  M) was added to an NaOH solution (pH = 9) at room-temperature  
435 to match the magnetite stoichiometry. The pH decrease associated with the release of protons  
436 from magnetite precipitation was compensated by adding additional NaOH solution (1 M) to  
437 keep the pH constant. The iron mixture, NaOH solution and magnetite synthesis solution

438 were kept under constant anoxic conditions by flushing N<sub>2</sub> to prevent oxidation. Magnetite  
439 samples were then recovered by centrifugation (8 000 rpm, 15 min), rinsed twice with Milli-  
440 Q water and dried in a dessicator to remove secondary minerals (*e.g.*, halite) precipitating  
441 from the sodium and chloride reactants reacting upon drying. MamP magnetite was  
442 produced following a similar protocol by adding an Fe(II)Cl<sub>2</sub> solution (0.1 M) as the sole  
443 iron source and MamP proteins (2 mg per mL) as the Fe(II)-oxidizing agent following a  
444 protocol previously established (4). All samples were kept under anoxic conditions before  
445 analyses.

446

#### 447 **Transmission electron microscopy**

448 Nanoparticles and bacterial samples were deposited on carbon-coated copper grids adapting  
449 a protocol described elsewhere (1). Chemical magnetite and bacteria were rinsed with Milli-  
450 Q water to remove salts precipitated from synthesis solutions and growth media. Samples  
451 were observed with a FEI Tecnai G2 Biotwin microscope operating at 100 kV. Particle sizes  
452 were measured with the ImageJ software.

453

#### 454 **X-ray Diffraction (XRD)**

455 XRD measurements were performed at the  $\mu$ Spot beamline at BESSY II synchrotron facility  
456 (Helmholtz Zentrum für Materialien and Energie, Berlin, Germany) (47). Measurements  
457 were carried out using a B34C/Mo Multilayer (2 nm period) monochromator and an energy  
458 of 15 keV. A sequence of pinholes was used to select a 100 x 100  $\mu\text{m}^2$  spot size. The data  
459 were normalized on primary beam intensity, and the background was subtracted.  
460 Transmission through the sample was calculated from an X-ray fluorescence signal collected

461 from a lead beamstop using a RAYSPEC Sirius SD-E65133-BE\_INC detector equipped  
462 with an 8  $\mu\text{m}$  beryllium window, where the primary beam intensity was monitored using an  
463 ion chamber. Diffraction data were collected by an Eiger 9 M detector with  $75 \times 75 \mu\text{m}^2$   
464 pixel area. Further data processing and reduction were done using the directly programmable  
465 data analysis kit (DPDAK) (51). Diffraction patterns were radially integrated and the  
466 scattered intensity  $I(Q)$  was calculated as a function of the momentum transfer  $Q$ , defined as  
467 :

$$468 \quad Q = \frac{4\pi}{\lambda} \sin\left(\frac{2\theta}{2}\right) \quad (1)$$

469 with  $\lambda$  and  $\theta$  being the photon wavelength and the scattering angle, respectively. The sample  
470 to detector distance was set to 189 mm and calibrated using quartz powder (NIST, standard  
471 reference material 1878a). Determination of peak position and particle size was performed  
472 following an established methodology with an in-house Python-based script exploiting the  
473 scipy library. Fits were performed by assuming a Pseudo-Voigt distribution and by taking  
474 into account experimental errors and instrumental broadening. All observed magnetite XRD  
475 peaks were fitted, but only those corresponding to the (311) magnetite reflection were taken  
476 into account in the present submission given that only such peak could be observed in  
477  $\Delta\text{mamP}$  AMB-1. For each sample, crystallite sizes were calculated from 360 XRD spectra  
478 (except for  $\Delta\text{mamP}$  AMB-1, which used 72 spectra).

479

## 480 **X-ray absorption spectroscopy (XAS) and X-ray magnetic circular dichroism (XMCD)** 481 **analyses**

482 XAS and XMCD measurements were performed at Soleil synchrotron facility (DEIMOS  
483 beamline equipped with a total electron yield detection method at 1 meV energy resolution)

484 at 3 K and under a magnetic field of 6 T. The beam size was  $800 \times 800 \mu\text{m}^2$ . Ferrihydrite  
485 reference material was precipitated following published methods (49). Its XAS and XMCD  
486 spectra match with previously published works (50, 51). Maghemite was obtained from  
487 oxidation of chemical magnetite by heating at  $120 \text{ }^\circ\text{C}$  in an oven for 48 h. Goethite XAS  
488 reference was provided by Dr. Victoria Coker (see ref. 47). Finally, Fe(III)-phosphate  
489 (tetrahydrated) powder was purchased from Sigma-Aldrich. All samples were stored under  
490 anoxic conditions for transportation to Soleil synchrotron. The DEIMOS beamline possesses  
491 a glove box for sample manipulation and mounting on sample holder in an oxygen-free  
492 environment. Samples were spread onto carbon tape on copper sample holders, which were  
493 then transferred to the superconducting magnet for loading in and acquisition of XAS and  
494 XMCD spectra. Data were obtained as previously described (53) by flipping both the  
495 circular polarization (left or right) and the orientation of the magnetic field being either  
496 parallel or anti-parallel to the photon propagation vector. XAS data were obtained by  
497 averaging two spectra corresponding to the left and right polarizations respectively, while  
498 XMCD spectra were calculated as the difference between the two when the magnetic field is  
499 applied in the direction of the incoming beam (perpendicular to the sample). XAS linear  
500 combinations were calculated with the Athena software using the Ifeffit package. The merit  
501 of goodness-of-fit (R-factor) was used to determine the best fits with lowest number of  
502 components (i.e., an additional component is only added to the fit if the goodness-to-fit  
503 value improves more than 10 %). XMCD spectra were fitted with theoretical spectra for  
504 each individual iron components (54).

505

506 **First-order reversal curves (FORC) measurements**

507 Magnetic properties of magnetite and bacterial samples were characterized with high-  
508 resolution FORC analyses using a vibrating-samples magnetometer (Lakeshore 8600 VSM).  
509 Samples were transferred in 1.5 mL-Eppendorf tubes and dried at room-temperature in a  
510 dessicator. High-resolution FORC measurements were performed in steps of 0.2 mT for all  
511 samples except chemical magnetite (0.4 mT), using a stepwise approach to the reversal field  
512 to avoid overshooting artifacts (55), and a pause of 3 s at reversal. Measurements have been  
513 processed with VARIFORC (56) using a variable smoothing approach that grants maximum  
514 resolution along  $B_c = 0$  and  $B_u = 0$ , for a correct characterization of the vertical ridge and the  
515 central ridge.

516

## 517 **Acknowledgements**

518 The authors would like to thank Magali Floriani from *Institut de Radioprotection et de*  
519 *Sûreté Nucléaire* (IRSN) for assistance with electron microscopy. Dr. Victoria Coker is also  
520 thanked for providing the goethite XAS reference. MA is supported by a grant through  
521 *Fondation pour la Recherche Médicale* (ARF201909009123). LM thanks the Horizon  
522 Europe Programme for the financial support provided through a Marie Skłodowska-Curie  
523 fellowship (101067742) and the BBVA Foundation for the Leonardo Fellowships for  
524 Researchers and Cultural Creators 2022. This work received support from Soleil synchrotron  
525 facility (DEIMOS beamline) under the awarded beamtime proposal #20210218.

526

## 527 **References**

528 1. D. Murat, A. Quinlan, H. Vali, A. Komeili, Comprehensive genetic dissection of  
529 the magnetosome gene island reveals the step-wise assembly of a prokaryotic organelle.  
530 *Proc. Natl. Acad. Sci. U. S. A.* **107**, 5593–5598 (2010).

- 531 2. W. Lin, *et al.*, Origin of microbial biomineralization and magnetotaxis during the  
532 Archean. *Proc. Natl. Acad. Sci. U. S. A.* **114**, 2171–2176 (2017).
- 533 3. R. Uebe, D. Schüler, Magnetosome biogenesis in magnetotactic bacteria. *Nat.*  
534 *Rev. Microbiol.* **14**, 621–637 (2016).
- 535 4. M. I. Siponen, *et al.*, Structural insight into magnetochrome-mediated magnetite  
536 biomineralization. *Nature* **502**, 681+ (2013).
- 537 5. S. R. Jones, *et al.*, Genetic and biochemical investigations of the role of MamP in  
538 redox control of iron biomineralization in *Magnetospirillum magneticum*. *Proc. Natl.*  
539 *Acad. Sci. U. S. A.* **112**, 3904–3909 (2015).
- 540 6. M. I. Siponen, G. Adryanczyk, N. Ginet, P. Arnoux, D. Pignol, Magnetochrome: a  
541 c-type cytochrome domain specific to magnetotactic bacteria. *Biochem. Soc. Trans.* **40**,  
542 1319–1323 (2012).
- 543 7. J. Baumgartner, *et al.*, Magnetotactic bacteria form magnetite from a phosphate-  
544 rich ferric hydroxide via nanometric ferric (oxyhydr)oxide intermediates. *Proc. Natl.*  
545 *Acad. Sci. U. S. A.* **110**, 14883–14888 (2013).
- 546 8. R. Uebe, *et al.*, Bacterioferritin of *Magnetospirillum gryphiswaldense* Is a  
547 Heterotetraicosameric Complex Composed of Functionally Distinct Subunits but Is Not  
548 Involved in Magnetite Biomineralization. *mBio* **10** (2019).
- 549 9. L. M. Fdez-Gubieda, *et al.*, Magnetite Biomineralization in *Magnetospirillum*  
550 *gryphiswaldense*: Time-Resolved Magnetic and Structural Studies. *ACS Nano* **7**, 3297–  
551 3305 (2013).
- 552 10. M. Amor, *et al.*, Defining Local Chemical Conditions in Magnetosomes of  
553 Magnetotactic Bacteria. *J. Phys. Chem. B* **126**, 2677–2687 (2022).
- 554 11. J. Baumgartner, M. A. Carillo, K. M. Eckes, P. Werner, D. Faivre, Biomimetic  
555 Magnetite Formation: From Biocombinatorial Approaches to Mineralization Effects.  
556 *Langmuir* **30**, 2129–2136 (2014).
- 557 12. A. Fischer, M. Schmitz, B. Aichmayer, P. Fratzl, D. Faivre, Structural purity of  
558 magnetite nanoparticles in magnetotactic bacteria. *J. R. Soc. Interface* **8**, 1011–1018  
559 (2011).
- 560 13. M. Amor, *et al.*, Magnetotactic Bacteria Accumulate a Large Pool of Iron Distinct  
561 from Their Magnetite Crystals. *Appl. Environ. Microbiol.* **86**, e01278-20 (2020).
- 562 14. S. Calvin, *et al.*, Comparison of extended x-ray absorption fine structure and  
563 Scherrer analysis of x-ray diffraction as methods for determining mean sizes of  
564 polydisperse nanoparticles. *Appl. Phys. Lett.* **87**, 233102 (2005).
- 565 15. F. Bourdelle, *et al.*, Quantification of the ferric/ferrous iron ratio in silicates by  
566 scanning transmission X-ray microscopy at the Fe L<sub>2,3</sub> edges. *Contrib Mineral Petrol*  
567 **166**, 423–434 (2013).
- 568 16. D. Faivre, L. H. Boettger, B. F. Matzanke, D. Schueler, Intracellular magnetite  
569 biomineralization in bacteria proceeds by a distinct pathway involving membrane-bound  
570 ferritin and an iron(II) species. *Angew. Chem.-Int. Edit.* **46**, 8495–8499 (2007).
- 571 17. D. M. Chevrier, *et al.*, Synchrotron-Based Nano-X-Ray Absorption Near-Edge  
572 Structure Revealing Intracellular Heterogeneity of Iron Species in Magnetotactic  
573 Bacteria. *Small Science* **2**, 2100089 (2022).
- 574 18. B. Moskowitz, R. Frankel, D. Bazylinski, Rock Magnetic Criteria for the  
575 Detection of Biogenic Magnetite. *Earth Planet. Sci. Lett.* **120**, 283–300 (1993).
- 576 19. P. Jungcharoen, *et al.*, Probing the effects of redox conditions and dissolved Fe<sup>2+</sup>

- 577 on nanomagnetite stoichiometry by wet chemistry, XRD, XAS and XMCD. *Environ.*  
578 *Sci.: Nano* **8**, 2098–2107 (2021).
- 579 20. R. Egli, “Magnetic characterization of geologic materials with first-order reversal  
580 curves” in *Magnetic Measurement Techniques for Materials Characterization*, V. Franco,  
581 B. Dodrill, Eds. (Springer, 2021).
- 582 21. Q. Liu, *et al.*, Characteristic low-temperature magnetic properties of aluminous  
583 goethite [ $\alpha$ -(Fe, Al)OOH] explained. *J. Geophys. Res.-Solid Earth* **111** (2006).
- 584 22. R. M. Cornell, U. Schwertmann, *The Iron Oxides: Structure, Properties,*  
585 *Reactions, Occurrences and Uses* (John Wiley & Sons, 2003).
- 586 23. A. R. Muxworthy, W. Williams, Critical superparamagnetic/single-domain grain  
587 sizes in interacting magnetite particles: implications for magnetosome crystals. *J. R. Soc.*  
588 *Interface* **6**, 1207–1212 (2009).
- 589 24. A. J. Newell, Transition to superparamagnetism in chains of magnetosome  
590 crystals. *Geochemistry, Geophysics, Geosystems* **10** (2009).
- 591 25. H. G. Katzgraber, *et al.*, Finite versus zero-temperature hysteretic behavior of spin  
592 glasses: Experiment and theory. *Phys. Rev. B* **76**, 092408 (2007).
- 593 26. C. Carvallo, S. Hickey, D. Faivre, N. Menguy, Formation of magnetite in  
594 Magnetospirillum gryphiswaldense studied with FORC diagrams. *Earth Planets Space*  
595 **61**, 143–150 (2009).
- 596 27. L. Chang, R. J. Harrison, T. A. Berndt, Micromagnetic simulation of  
597 magnetofossils with realistic size and shape distributions: Linking magnetic proxies with  
598 nanoscale observations and implications for magnetofossil identification. *Earth Planet.*  
599 *Sci. Lett.* **527**, 115790 (2019).
- 600 28. M. Kumari, *et al.*, Experimental mixtures of superparamagnetic and single-  
601 domain magnetite with respect to Day-Dunlop plots. *Geochem. Geophys. Geosyst.* **16**,  
602 1739–1752 (2015).
- 603 29. A. Olszewska-Widdrat, G. Schiro, V. E. Reichel, D. Faivre, Reducing Conditions  
604 Favor Magnetosome Production in Magnetospirillum magneticum AMB-1. *Front.*  
605 *Microbiol.* **10**, 582 (2019).
- 606 30. A. Lohße, *et al.*, Genetic Dissection of the mamAB and mms6 Operons Reveals a  
607 Gene Set Essential for Magnetosome Biogenesis in Magnetospirillum gryphiswaldense. *J*  
608 *Bacteriol* **196**, 2658–2669 (2014).
- 609 31. R. Uebe, *et al.*, The cation diffusion facilitator proteins MamB and MamM of  
610 Magnetospirillum gryphiswaldense have distinct and complex functions, and are involved  
611 in magnetite biomineralization and magnetosome membrane assembly. *Mol. Microbiol.*  
612 **82**, 818–835 (2011).
- 613 32. L. Kuhrts, E. Macías-Sánchez, N. V. Tarakina, A. M. Hirt, D. Faivre, Shaping  
614 Magnetite with Poly-l-arginine and pH: From Small Single Crystals to Large  
615 Mesocrystals. *J. Phys. Chem. Lett.* **10**, 5514–5518 (2019).
- 616 33. J. Li, W. Wu, Q. Liu, Y. Pan, Magnetic anisotropy, magnetostatic interactions and  
617 identification of magnetofossils. *Geochem. Geophys. Geosyst.* **13**, Q10Z51 (2012).
- 618 34. O. Raschdorf, *et al.*, A quantitative assessment of the membrane-integral sub-  
619 proteome of a bacterial magnetic organelle. *Journal of Proteomics* **172**, 89–99 (2018).
- 620 35. J. Werckmann, *et al.*, Localized iron accumulation precedes nucleation and  
621 growth of magnetite crystals in magnetotactic bacteria. *Sci Rep* **7**, 8291 (2017).
- 622 36. D. M. Hershey, *et al.*, MamO Is a Repurposed Serine Protease that Promotes

623 Magnetite Biomineralization through Direct Transition Metal Binding in Magnetotactic  
624 Bacteria. *PLOS Biology* **14**, e1002402 (2016).

625 37. H. Nudelman, *et al.*, Structure-function studies of the magnetite-biomineralizing  
626 magnetosome-associated protein MamC. *J. Struct. Biol.* **194**, 244–252 (2016).

627 38. E. Cornejo, P. Subramanian, Z. Li, G. J. Jensen, A. Komeili, Dynamic  
628 Remodeling of the Magnetosome Membrane Is Triggered by the Initiation of  
629 Biomineralization. *mBio* **7**, e01898-15 (2016).

630 39. Y. Li, E. Katzmann, S. Borg, D. Schueler, The Periplasmic Nitrate Reductase Nap  
631 Is Required for Anaerobic Growth and Involved in Redox Control of Magnetite  
632 Biomineralization in *Magnetospirillum gryphiswaldense*. *J. Bacteriol.* **194**, 4847–4856  
633 (2012).

634 40. U. Dippon, C. Pantke, K. Porsch, P. Larese-Casanova, A. Kappler, Potential  
635 Function of Added Minerals as Nucleation Sites and Effect of Humic Substances on  
636 Mineral Formation by the Nitrate-Reducing Fe(II)-Oxidizer *Acidovorax* sp BoFeN1.  
637 *Environ. Sci. Technol.* **46**, 6556–6565 (2012).

638 41. H. A. Crosby, E. E. Roden, C. M. Johnson, B. L. Beard, The mechanisms of iron  
639 isotope fractionation produced during dissimilatory Fe(III) reduction by *Shewanella*  
640 *putrefaciens* and *Geobacter sulfurreducens*. *Geobiology* **5**, 169–189 (2007).

641 42. M. Amor, M. Tharaud, A. Gélabert, A. Komeili, Single-cell determination of iron  
642 content in magnetotactic bacteria: implications for the iron biogeochemical cycle.  
643 *Environ. Microbiol.* **22**, 823–831 (2020).

644 43. O. Raschdorf, F. D. Mueller, M. Posfai, J. M. Plitzko, D. Schueler, The  
645 magnetosome proteins MamX, MamZ and MamH are involved in redox control of  
646 magnetite biomineralization in *Magnetospirillum gryphiswaldense*. *Mol. Microbiol.* **89**,  
647 872–886 (2013).

648 44. J. Wan, *et al.*, A protease-mediated switch regulates the growth of magnetosome  
649 organelles in *Magnetospirillum magneticum*. *Proc. Natl. Acad. Sci. U. S. A.* **119** (2022).

650 45. J. Wan, *et al.*, McaA and McaB control the dynamic positioning of a bacterial  
651 magnetic organelle. *Nat Commun* **13**, 5652 (2022).

652 46. A. Komeili, H. Vali, T. J. Beveridge, D. K. Newman, Magnetosome vesicles are  
653 present before magnetite formation, and MamA is required for their activation. *Proc.*  
654 *Natl. Acad. Sci. U. S. A.* **101**, 3839–3844 (2004).

655 47. I. Zizak, The mySpot beamline at BESSY II. *Journal of large-scale research*  
656 *facilities JLSRF* **2**, 102 (2016).

657 48. G. Benecke, *et al.*, A customizable software for fast reduction and analysis of  
658 large X-ray scattering data sets: applications of the new DPDAK package to small-angle  
659 X-ray scattering and grazing-incidence small-angle X-ray scattering. *J Appl Cryst* **47**,  
660 1797–1803 (2014).

661 49. T. D. Waite, J. A. Davis, T. E. Payne, G. A. Waychunas, N. Xu, Uranium(VI)  
662 adsorption to ferrihydrite: Application of a surface complexation model. *Geochim.*  
663 *Cosmochim. Acta* **58**, 5465–5478 (1994).

664 50. Y. Guyodo, *et al.*, X-ray magnetic circular dichroism provides strong evidence for  
665 tetrahedral iron in ferrihydrite. *Geochem. Geophys. Geosyst.* **13** (2012).

666 51. M. Sassi, *et al.*, Influence of time and ageing conditions on the properties of  
667 ferrihydrite. *Environ. Sci.: Nano* **11**, 1682–1692 (2024).

668 52. V. S. Coker, *et al.*, Bacterial production of vanadium ferrite spinel (Fe,V)3O4

669 nanoparticles. *Am. Miner.* **84**, 554–562 (2020).  
670 53. J. Li, *et al.*, Controlled cobalt doping in the spinel structure of magnetosome  
671 magnetite: new evidences from element- and site-specific X-ray magnetic circular  
672 dichroism analyses. *J. R. Soc. Interface* **13**, 20160355 (2016).  
673 54. R. A. D. Patrick, *et al.*, Cation site occupancy in spinel ferrites studied by X-ray  
674 magnetic circular dichroism: Developing a method for mineralogists. *Eur. J. Mineral.* **14**,  
675 1095–1102 (2002).  
676 55. C. L. Wagner, *et al.*, Diversification of Iron-Biomineralizing Organisms During  
677 the Paleocene-Eocene Thermal Maximum: Evidence From Quantitative Unmixing of  
678 Magnetic Signatures of Conventional and Giant Magnetofossils. *Paleoceanogr.*  
679 *Paleoclimatol.* **36**, e2021PA004225 (2021).  
680 56. R. Egli, VARIFORC: An optimized protocol for calculating non-regular first-  
681 order reversal curve (FORC) diagrams. *Global and Planetary Change* **110**, 302–320  
682 (2013).

683  
684  
685  
686

## 687 **Figure legends**

688 **Fig. 1** X-ray diffractograms of (A) MamP magnetite and WT AMB-1, and (B)  $\Delta mamP$   
689 AMB-1. Chemical magnetite is given as a reference on both panels. All peaks can be  
690 attributed to magnetite - M, goethite - G and halite - H. Inset on panel (B) highlights the  
691 (311) magnetite reflection in  $\Delta mamP$  samples.

692  
693 **Fig. 2** (A, C, E) Fe  $L_3$ -edge X-ray absorption spectra of chemical magnetite (black),  
694 MamP magnetite (light brown), WT AMB-1 (blue) and  $\Delta mamP$  AMB-1 (red). (B, D)  
695 Linear combinations fitting the spectra of WT AMB-1 (blue) and  $\Delta mamP$  AMB-1 (red):  
696 magnetite = 30%, maghemite = 40% and ferrihydrite = 30%. (F) Linear combination  
697 fitting the spectrum of MamP magnetite: maghemite = 55 %, goethite = 37 % and MamP  
698 proteins = 8 %. The Fe  $L_2$ -edge spectra of all samples and references are also provided in  
699 supporting materials (Fig. S9).

700

701 **Fig. 3** Fe  $L_3$ -edge X-ray magnetic circular dichroism spectra of chemical magnetite  
702 (black), MamP magnetite (light brown), and bacterial samples (i.e., WT AMB-1 in blue  
703 and  $\Delta mamP$  AMB-1 in red) acquired at 3 and 300 K. The Fe  $L_2$ -edge spectra of all  
704 samples and references are also provided in supporting materials (Fig. S10).

705

706 **Fig. 4** First-order reversal curves diagrams of (A) chemical magnetite, (B) MamP  
707 magnetite, (C)  $\Delta mamP$  AMB-1 and (D) WT AMB-1 cells. Quantile contours enclose  
708 regions associated with a fraction  $1 - Q$  of the total magnetization represented by the  
709 diagram. Insets show the major hysteresis loop, which is the envelope of all  
710 measurements. Numbers near the contours inside the plots are quantiles  $< 10\%$  that  
711 cannot be resolved in the color bar.

712

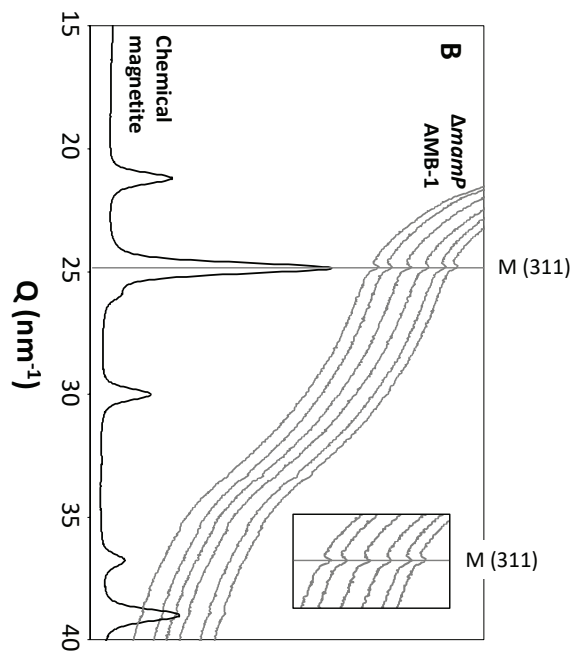
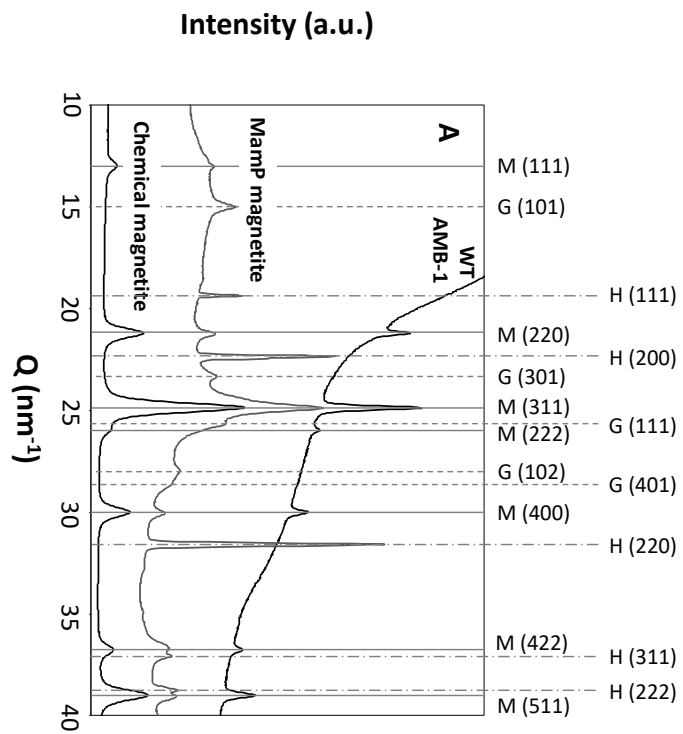
713 **Fig. 5** (A-B) Transmission electron microscopy of (A) wild-type and (B)  $\Delta mamP$  AMB-  
714 1. Inset in (A) highlights magnetite in WT AMB-1 (scale bar = 100 nm). Inset in (B)  
715 magnifies small particles (scale bar = 50 nm). (C-D) Size of magnetite nanoparticles in  
716 (C) WT and (D)  $\Delta mamP$  AMB-1 measured by transmission electron microscopy.  $S$  refers  
717 to the shape factor describing the particle elongation and calculated as  $S = \text{width}/\text{length}$ .

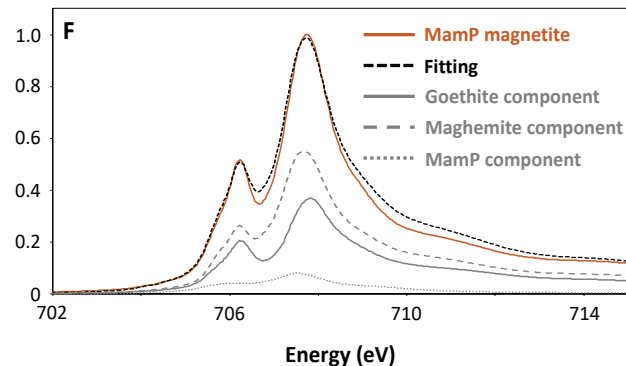
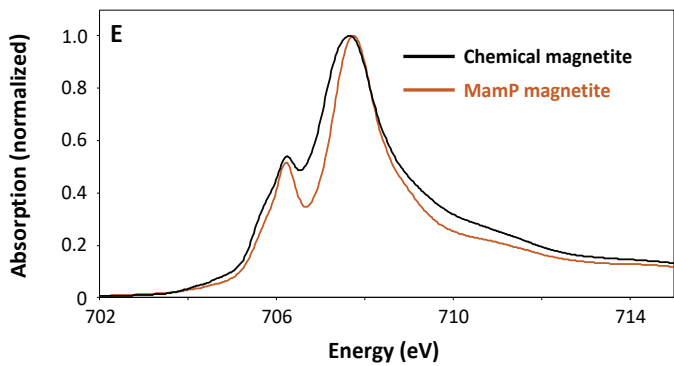
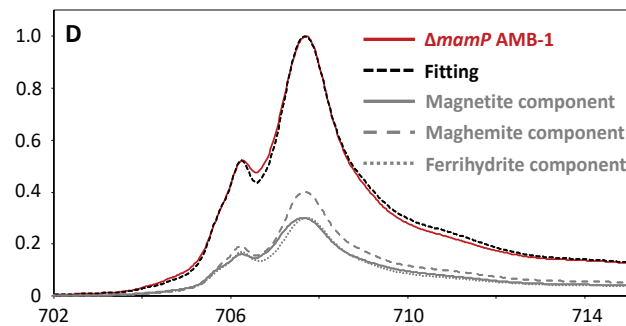
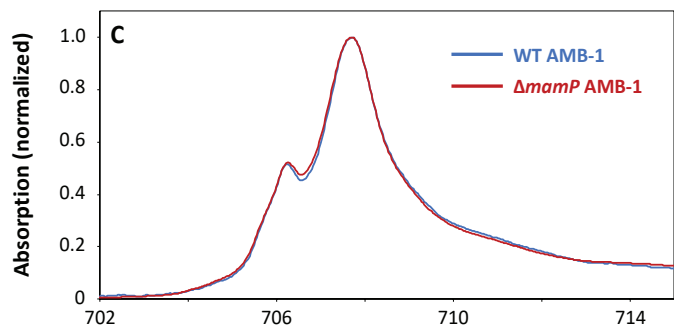
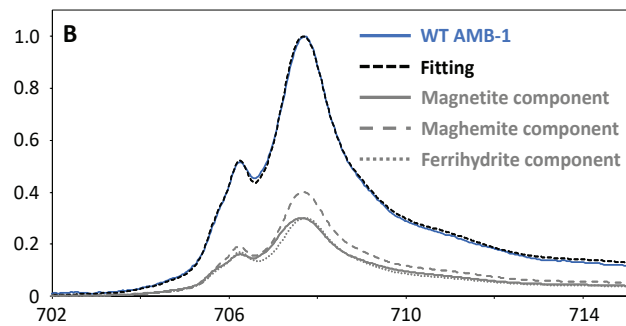
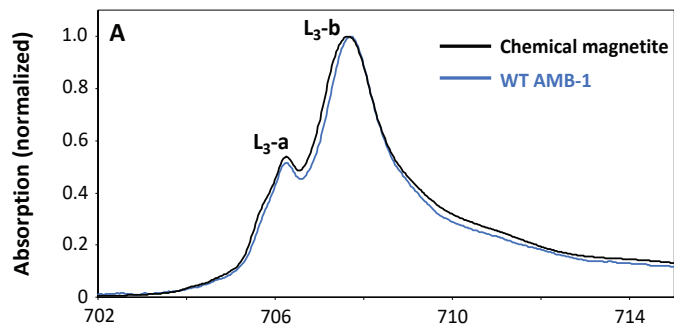
718

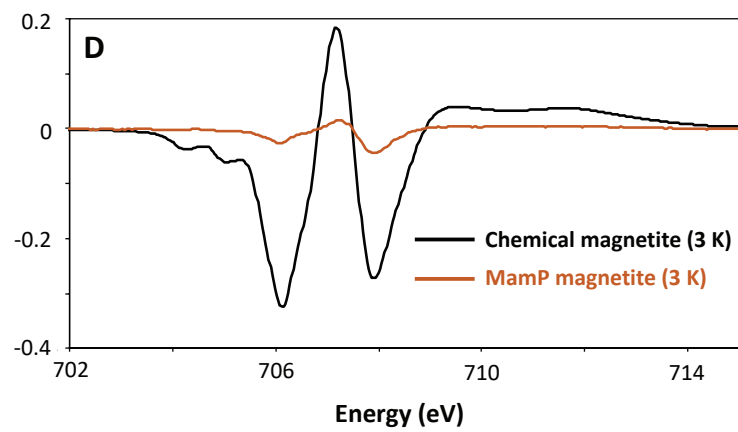
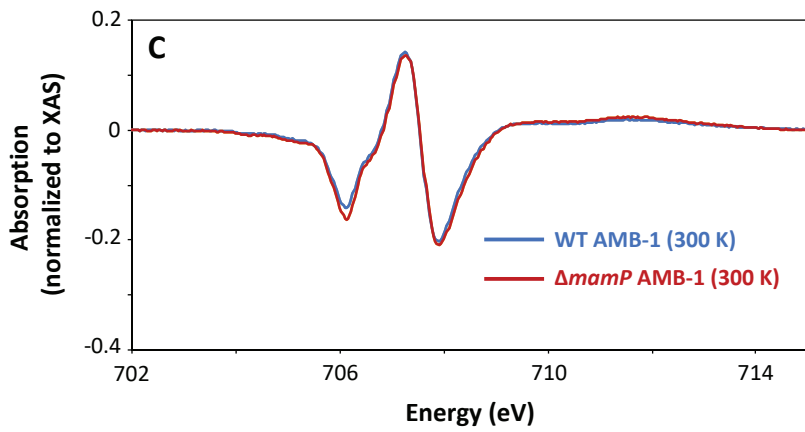
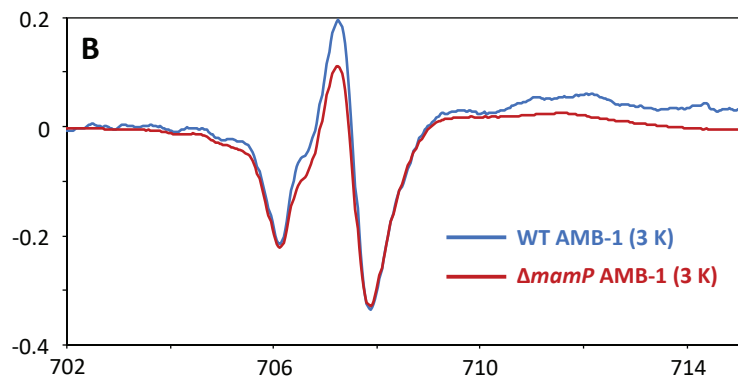
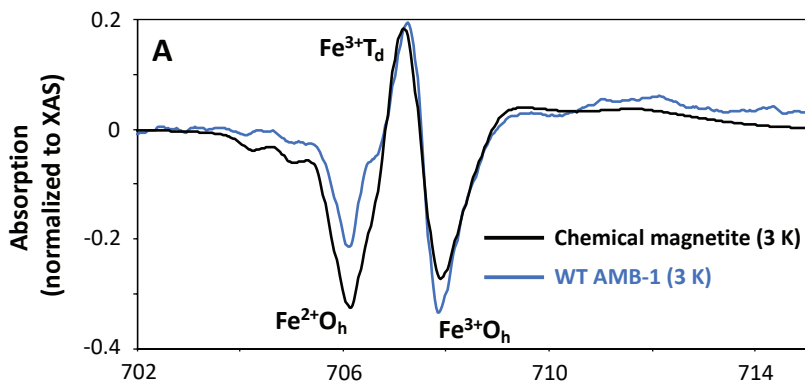
719 **Fig. 6** Proposed model for MamP function in magnetite biomineralization. Eh: redox  
720 potential.  $\text{Fe(II)}_{\text{aq}}$ : aqueous Fe(II) species.  $\text{Fe(II)}_{\text{sorb}}$ : Fe(II) adsorbed on the magnetite  
721 nanoparticle. See main text for a detailed description of the model.

722

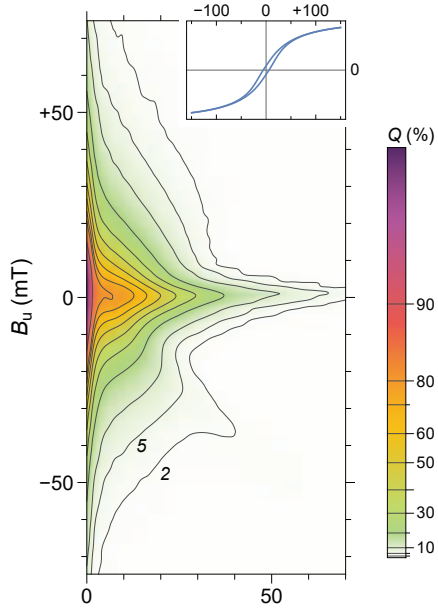
723 **Fig. 7** Number of WT-like nanoparticles in  $\Delta mamP$  AMB-1 represented against the  
724 number of total nanoparticles observed in the same cells with electron microscopy.



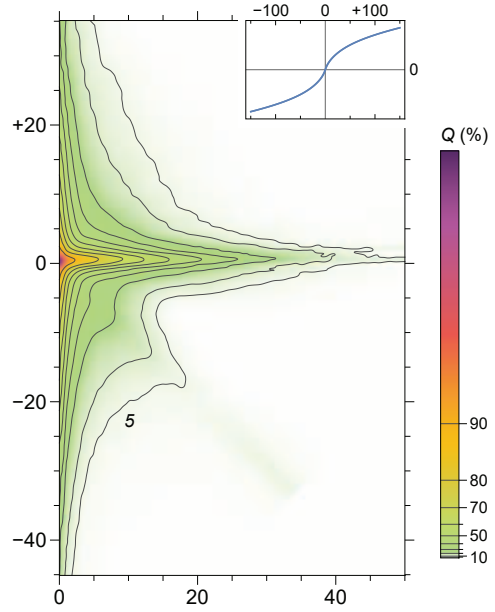




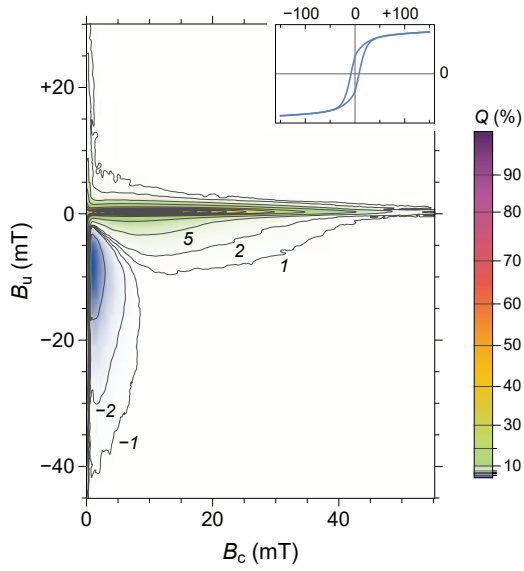
**A** Chemical magnetite



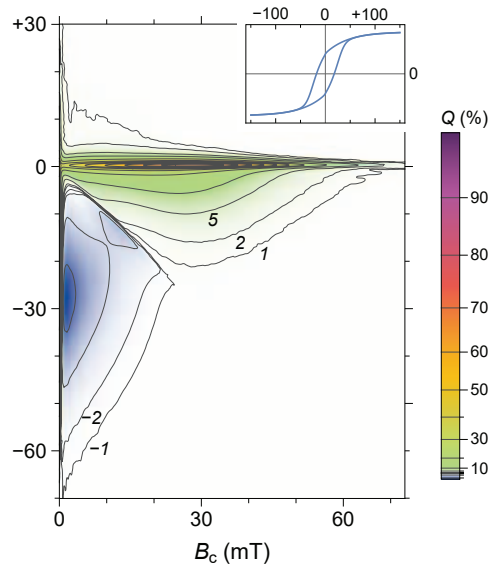
**B** MamP magnetite

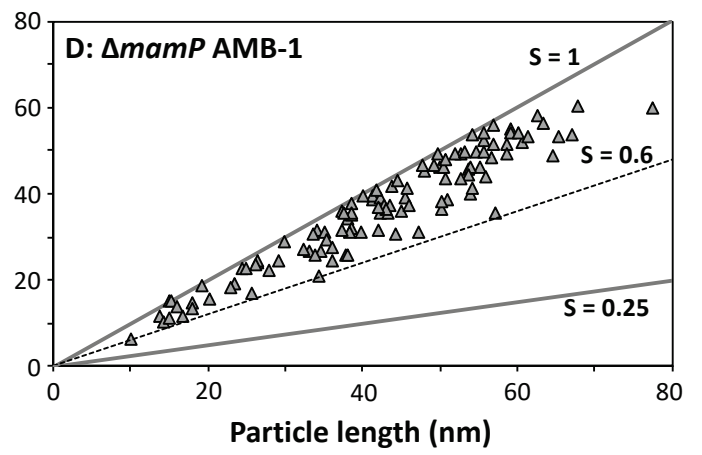
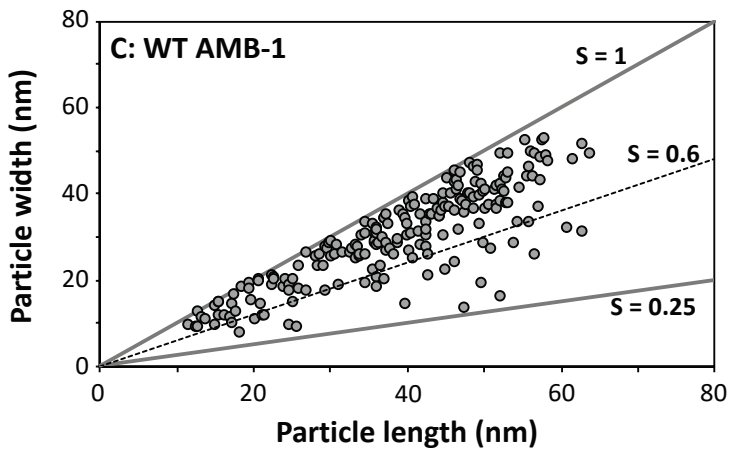
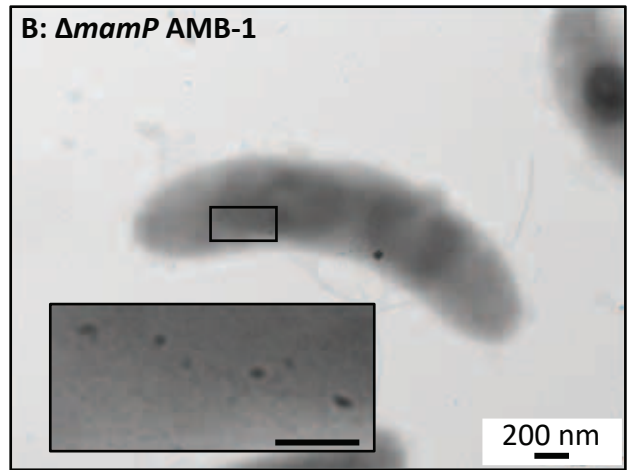
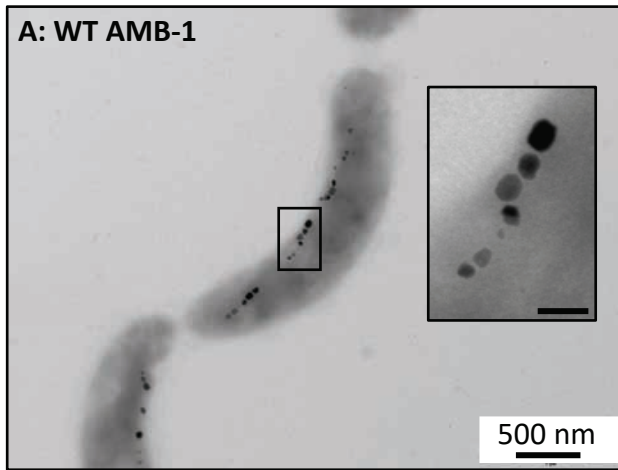


**C**  $\Delta$ mamP AMB-1



**D** WT AMB-1



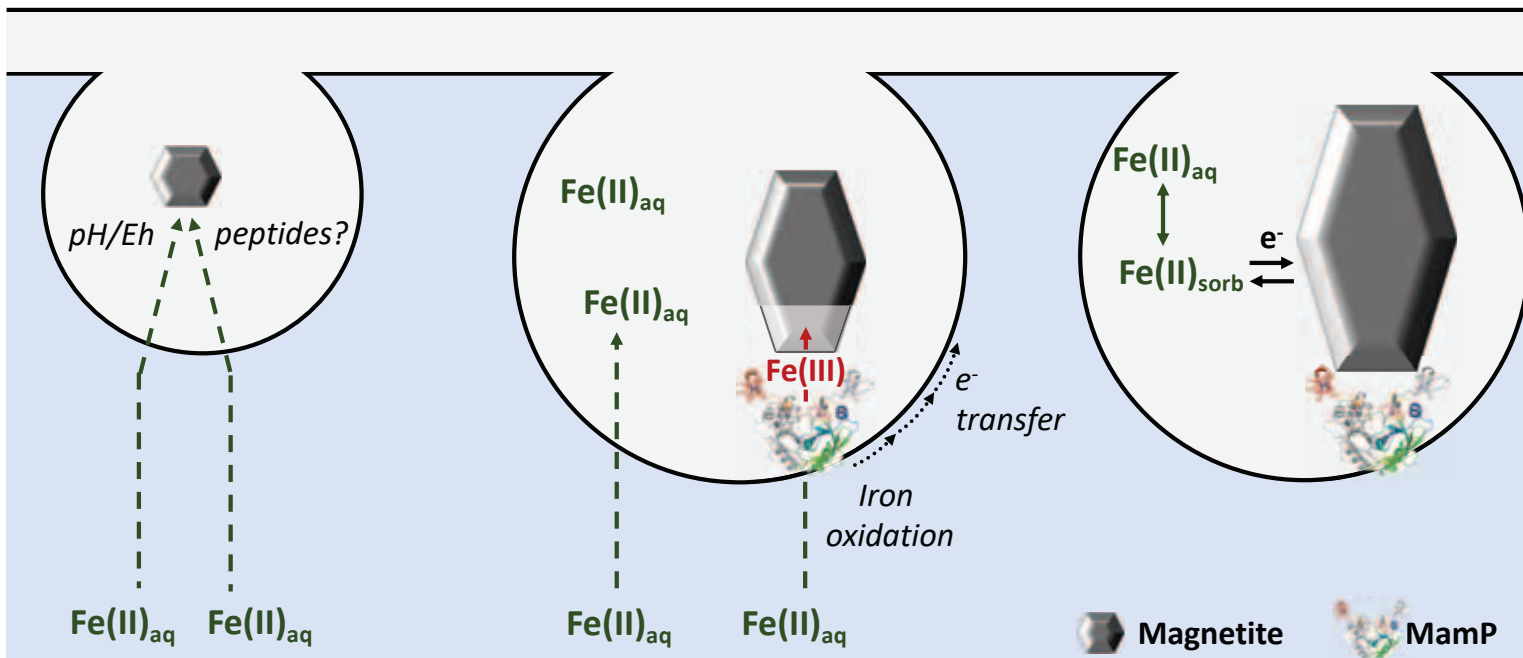


Periplasm  
Cytoplasm

**Step 1**  
*Magnetite nucleation  
in magnetosomes*

**Step 2**  
*Incorporation of Fe(III)  
into magnetite by MamP*

**Step 3**  
*Fe(II) adsorption and electron  
transfer to magnetite*



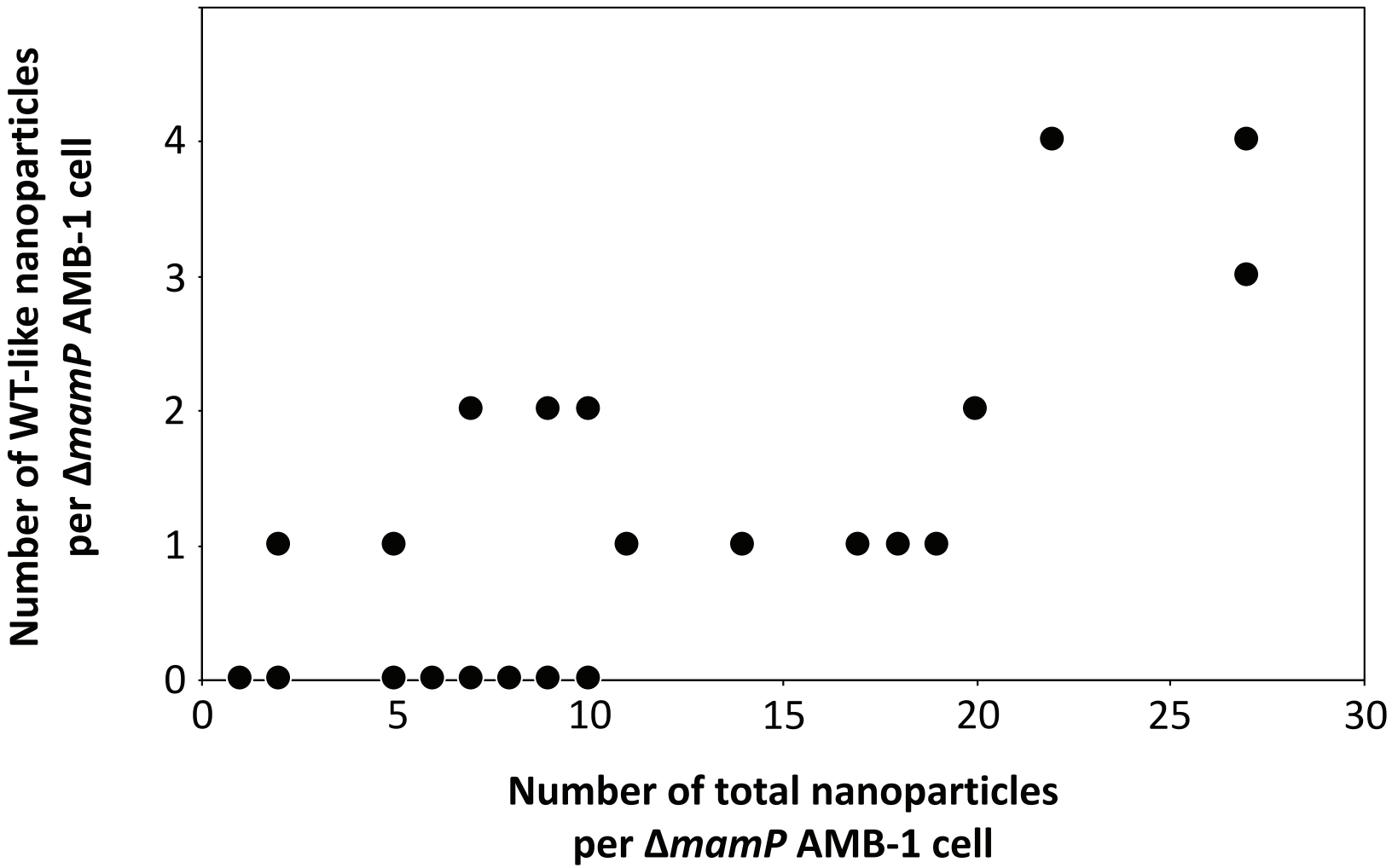


**Table 1.** Size and volume of superparamagnetic (SP, length < 18 and 25 nm for WT and  $\Delta mamP$  AMB-1, respectively, see main text) and stable single-domain (SSD) magnetite nanoparticles synthesized in WT and  $\Delta mamP$  AMB-1 and measured from electron microscopy.

	WT AMB-1		$\Delta mamP$ AMB-1	
	SP	SSD	SP	SSD
Mean length (L) (nm)	15	41	12	46
Shape factor (S)	0.79	0.78	0.85	0.86
Mean volume per particle (nm <sup>3</sup> )	1 102	21 944	657	37 287
Fraction of the total number of particles in the cell (%)	25	75	90	10
Fraction of the total volume (%)	2	98	14	86